

Atomic-scale homogeneous plastic flow beyond near-theoretical yield stress in a metallic glass

Jiaxin Yu^{1,2}, Amit Datye², Zheng Chen², Chao Zhou², Omur E. Dagdeviren^{2,4}, Jan Schroers² & Udo D. Schwarz^{2,3}

The onset of yielding and the related atomic-scale plastic flow behavior of bulk metallic glasses at room temperature have not been fully understood due to the difficulty in performing the atomic-scale plastic deformation experiments needed to gain direct insight into the underlying fundamental deformation mechanisms. Here we overcome these limitations by combining a unique sample preparation method with atomic force microscopy-based indentation, which allows study of the yield stress, onset of yielding, and atomic-scale plastic flow of a platinum-based bulk metallic glass in volumes containing as little as approximately 1000 atoms. Yield stresses markedly higher than in conventional nanoindentation testing were observed, surpassing predictions from current models that relate yield stress to tested volumes; subsequent flow was then established to be homogeneous without exhibiting collective shear localization or loading rate dependence. Overall, variations in glass properties due to fluctuations of free volume are found to be much smaller than previously suggested.

¹Key Laboratory of Testing Technology for Manufacturing Process in Ministry of Education, State Key Laboratory of Environment-friendly Energy Materials, Southwest University of Science and Technology, Mianyang, China. ²Department of Mechanical Engineering and Materials Science, Yale University, New Haven, CT, USA. ³Department of Chemical and Environmental Engineering, Yale University, New Haven, CT, USA. ⁴Present address: Department of Mechanical Engineering, École de technologie supérieure, University of Quebec, Montreal, Quebec H3C 1K3, Canada.
email: yujiaxin@swust.edu.cn; udo.schwarz@yale.edu

With the advent of an ability to produce amorphous metallic alloys in bulk quantities, their distinct mechanical behavior has opened up exciting application opportunities¹. However, the poor room temperature plasticity of these so-called bulk metallic glasses (BMGs) impedes many engineering applications, which is why understanding their plastic deformation and flow mechanism has received much attention^{2–4}. The room temperature plastic flow of BMG is usually inhomogeneous, which manifests as serrated stress–strain curves during uniaxial tensile/compressive tests in macroscopic specimens^{3–5} and in conventional nanoindentation experiments using indenter radii of ≈ 0.2 – $10\ \mu\text{m}$ ^{6,7}. Each serration corresponds to the formation of a single shear band or the formation and evolution of multiple shear bands, which represent the processes that are thought to govern the yielding and plasticity of BMGs at room temperature^{8,9}. Owing to the coordinated deformation of multiple shear bands, the maximum shear stress occurring at yield in uniaxial tension/compression tests was found to be $\sim 2.5\%$ of the shear modulus G of the material (or $G/40$) based on tests conducted on >30 BMGs of different compositions, with G representing their respective shear modulus¹⁰. During conventional nanoindentation, the formation of the first shear band, detected by the first pop-in event in the force vs penetration depth curve, is considered as the onset of plastic deformation of BMGs. When doing so, a yield shear stress in a range of $G/20$ to $G/10$ is observed^{11,12}, much higher than under uniaxial tension/compression. This has been explained by the smaller volumes affected during nanoindentation experiments compared with uniaxial compression tension experiments of bulk samples, which reduces the number of shear bands that are able to nucleate¹¹. Another argument is that the larger the specimens, the larger the population of defects is that they contain. With failure being determined by the weakest link, the smaller the stressed volume, the lower the probability for the volume to include a particularly weak link, which ultimately results in higher shear stresses¹³. However, even though there is a difference in the stressed volume between conventional nanoindentation and uniaxial tension/compression testing, the plastic deformation of BMGs is in both situations controlled by shear band dynamics. The question therefore arises: What happens if the stressed volume becomes too small for shear bands to form?

Here, we address this issue by investigating plastic flow in volumes containing as little as 1000 atoms, a number so small that it impedes all previously considered modes of collective shearing. We achieve this by using virtually atomically flat BMG samples, prepared from a $\text{Pt}_{57.5}\text{Cu}_{14.7}\text{Ni}_{5.3}\text{P}_{22.5}$ alloy¹⁴ (Pt-BMG) via thermoplastic forming^{15,16}. The onset of yielding and plastic flow at the atomic scale is then investigated with atomic force microscopy (AFM)-based nanoindentation providing the desired localization. We find much higher yield stresses compared with the values obtained by conventional nanoindentation testing, after which virtually homogeneous plastic flow without exhibiting any loading rate dependence within the parameter range covered is observed. Representing the smallest-scale mechanical deformation testing to date on BMGs, the results provide important insights to understanding plastic deformation mechanism of BMGs at the atomic scale. Perhaps even more notably, our results do not reveal any variations in properties on the length scale of observation, which is distinct from expectations based on previous concepts describing inhomogeneity in metallic glasses^{17–21}. As a consequence, our findings may affect the establishment of structure-property-processing relationships in metallic glasses, where proposed toughening and strain hardening mechanisms typically assume a heterogeneous structure^{22,23}.

Results and discussion

Conventional nanoindentation. By averaging data obtained from 15 individual indentations using a Berkovich indenter on Pt-BMG samples prepared following the thermoplastic forming procedure explained in the Methods section, the elastic modulus of the BMG E_{BMG} was determined to be (105 ± 5) GPa. Measurements were performed at five different loading rates ranging from $0.5\ \text{mNs}^{-1}$ to $15\ \text{mNs}^{-1}$, with three curves being recorded at each rate. Even though loading curves changed from smooth to serrated with decreasing speed, the value of E_{BMG} extracted from the individual curves did not exhibit any noticeably loading rate dependency (Supplementary Materials Fig. 1). With Poisson's ratio $\nu = 0.39$ ²⁴, the shear modulus of Pt-BMG was then calculated from $G = E/2(1 + \nu)$ as $G = (37.8 \pm 1.8)$ GPa, which is the number used throughout this paper. It is, however, worth noting that this value is higher than the 33.3 GPa measured using ultrasonic methods with bulk Pt-BMG¹⁴.

In contrast to nanoindentation with a pyramidal Berkovich tip where plastic flow is expected to occur almost immediately, nanoindentation with spherical tips is known to be elastic until the first pop-in event is registered, which then indicates the occurrence of the first shear band^{8,25} and thus the onset of plastic deformation. Therefore, 30 separate indents were carried out using a spherical diamond tip featuring a radius of ≈ 320 nm to study flow, with Fig. 1a showing a typical force F vs penetration depth h curve. By averaging, the critical depth h_y and critical load F_y when yielding occurs were found to be (10.4 ± 2) nm and (0.11 ± 0.02) mN; when h and F are lower than these critical values, the load–depth response follows the Hertzian elastic prediction (dashed blue curve)²⁶.

A statistical analysis for the critical (i.e., yield) shear stresses occurring at the first pop-in event τ_y is then presented in Fig. 1b. All values for τ_y are within the range of 3.51 – 4.62 GPa, which corresponds to a band confined by $\tau_{y,\text{min}} \approx G/11$ and $\tau_{y,\text{max}} \approx G/8$ with the averaged value being (4.06 ± 0.32) GPa or $\approx G/9$. In contrast, statistical analysis for the yield shear stresses occurring at the first pop-in event τ_y for complementary nanoindentation experiments performed on Pt-BMG samples with spherical diamond tips of radii $\approx 1.7\ \mu\text{m}$ and $\approx 7.5\ \mu\text{m}$ results in averaged values of (3.19 ± 0.21) GPa (i.e., $\approx G/12$) and (2.44 ± 0.26) GPa ($\approx G/16$), respectively.

Characterization of samples prepared by thermoplastic forming.

Samples prepared using the thermoplastic imprinting approach described in the Materials and Methods section¹⁵ to reflect mirror images of the SrTiO_3 (STO) crystals employed as mold were characterized by tapping-mode AFM, with an example shown in Fig. 2. The widths of the terraces formed on the Pt-BMG replicas were found to be between 50 nm and 400 nm with the height differences between two terraces being (0.39 ± 0.02) nm, which reflects one-unit cell on the STO's (001) surface. In addition, the root-mean-square (RMS) roughness on individual terraces was quantified on numerous locations and samples as ≈ 0.10 nm or less; the RMS roughness within the box marked in Fig. 2a, e.g., was found to be 0.057 nm.

To investigate the influence of structural inhomogeneities, a phase image of the same area as in Fig. 2a is displayed in Fig. 2b. If such inhomogeneities were to be significant, they should cause a contrast in-phase images, which are known to reflect local variations in viscoelasticity²⁷. However, even though previous researchers have reported noticeable phase contrasts^{28,29}, we see only minimal phase fluctuation. As an example, the RMS variation of the phase values inside the box marked in Fig. 2b is found to be 1.06° , indicating that the effect of structural inhomogeneities on local indentations should be negligible. We

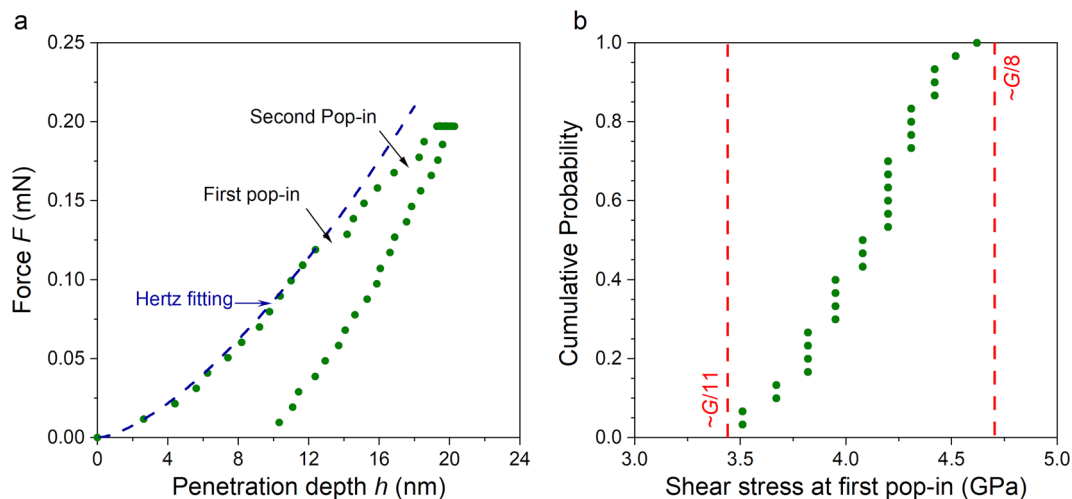


Fig. 1 Assessing the mechanical properties of Pt-BMG with conventional nanoindentation. **a** Typical force vs penetration depth curve measured on Pt-BMG with a commercial nanoindenter using a 320 nm radius spherical diamond tip. The loading rate was set as $50 \mu\text{Ns}^{-1}$. The Hertz fitting curve (dashed blue curve) is obtained with Eq. (1) from the Materials and Methods section. **b** Cumulative distribution function visualizing the scatter of the yield shear stress τ_y , obtained from analyzing 30 distinct nanoindentations on Pt-BMG using the same experimental protocol as in **a**; note that the pop-in loads measured were determined only up to one decimal place, which is why the shear stress at first pop-in is the same value for multiple indentation experiments. Nevertheless, all values found are within a band limited by $G/11$ and $G/8$.

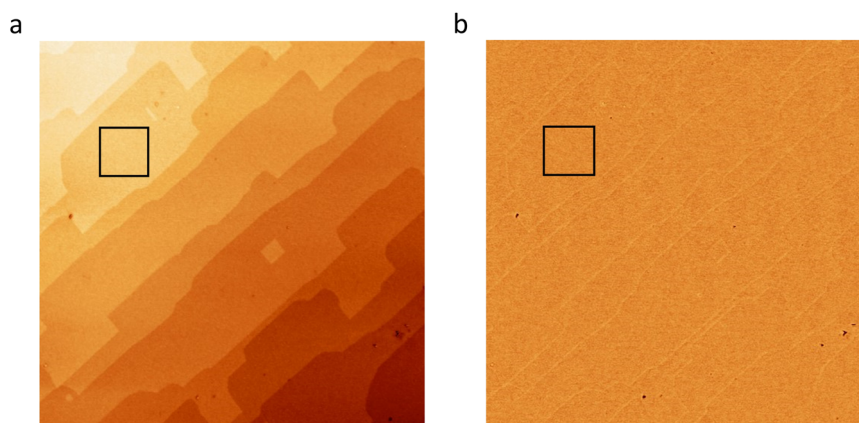


Fig. 2 Characterization of virtually atomically flat Pt-BMG sample surfaces using tapping-mode atomic force microscopy. **a** Topography of a Pt-BMG sample prepared by thermoplastic forming; image size is $2 \mu\text{m} \times 2 \mu\text{m}$. The surface, which represents an exact mirror image of the STO surface used as a mold during the imprinting, features flat terraces separated by steps of 0.39 nm height, and the RMS roughness within the $250 \text{ nm} \times 250 \text{ nm}$ box was computed to be 0.057 nm. **b** Phase image of the same area as in **a**. While step edges cause topography-induced variations in phase, its value fluctuates one minimally on terraces (e.g., by 1.06° RMS inside the box).

speculate that this divergence from the earlier reported results is due to the fact that our samples are 1–2 orders of magnitude smoother, thereby reducing the chance of surface imperfections and/or topographical changes interfering with the data acquisition. In addition, it is also possible that the thermoplastic forming process results in a structurally more homogeneous state than previous preparation methods.

AFM-based indentation. AFM-based nanoindentation techniques^{30,31} can produce stressed volumes in BMGs at the atomic scale without a need to decrease the sample's dimensions. AFM-based nanoindentation, which benefits from high force resolution ($\sim\text{nN}$), displacement resolution ($\sim\text{sub-angstrom}$), and sharp indenting tips (radii of typically a few nm), has previously been employed to investigate the atomic-scale yield, dislocation nucleation, and single-glide events in crystalline materials^{32–34}, but has thus far rarely been applied to study BMGs³⁵. This

underuse originates from the fact that for a meaningful analysis of indentation tests, the dimensional uncertainty originating from surface roughness needs to be considerably lower than the probing volume. In this context, this means that the surface must effectively be “atomically flat” for artifact-free data interpretation. Although such “atomically flat” surfaces have been difficult to achieve with BMGs surfaces in the past, thermoplastically formed samples such as the one characterized in the previous section are ideally suited, with data obtained from indentations with depths larger than $\approx 1 \text{ nm}$ being unaffected by surface roughness.

Three diamond tips, labeled as #1, #2, and #3, of tip radii specified by the manufacturer as $<10 \text{ nm}$, were used to perform AFM indentation tests on two distinct thermoplastically formed Pt-BMG samples (samples #1 and #2). The indentation tests shown in Fig. 3a was recorded with tip #1 on sample #1, whereas the data from Fig. 3b, c, performed with tips #2 and #3, respectively, was acquired in both cases on sample #2. The respective F – h loading curves can be divided into two segments.

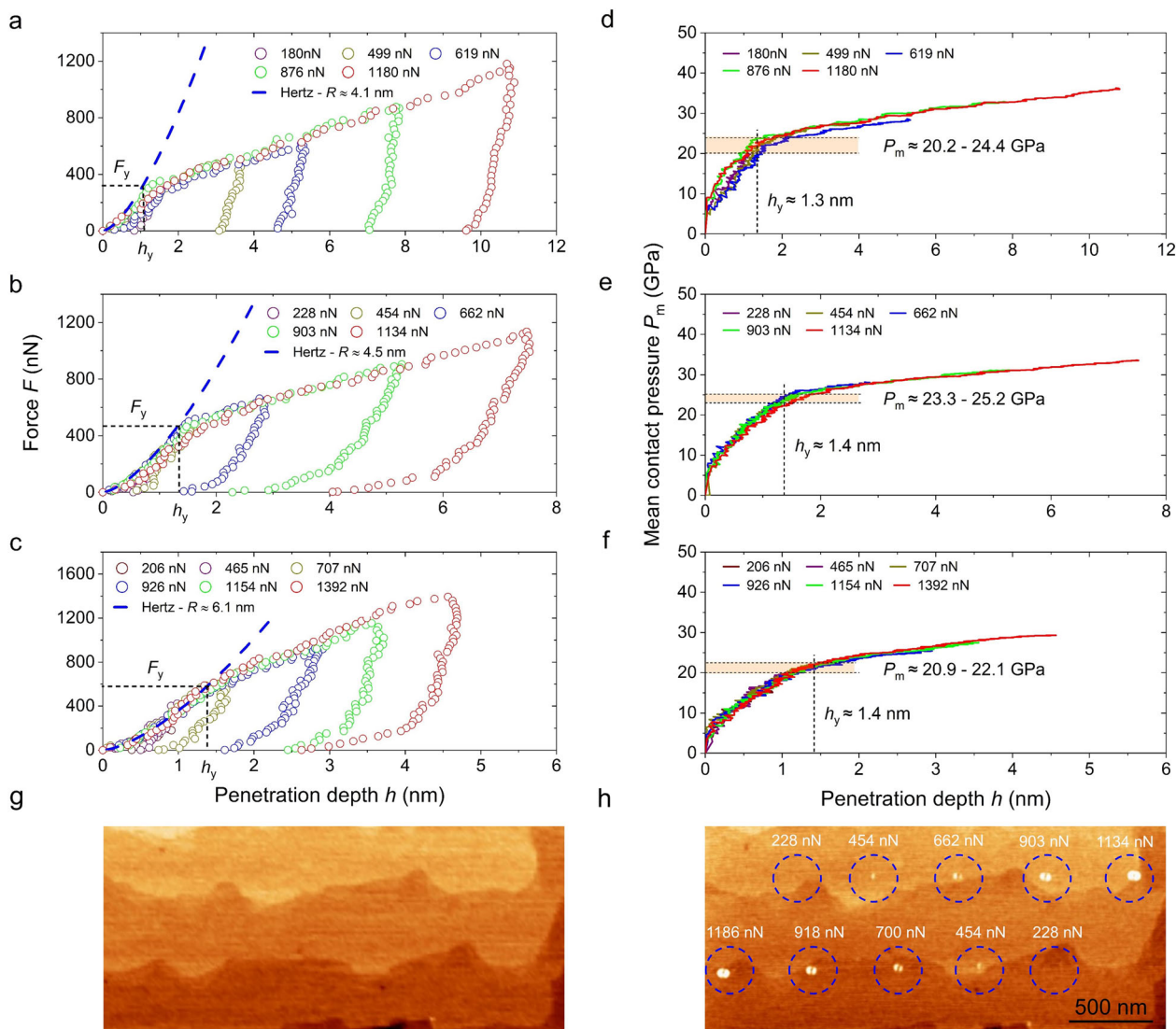


Fig. 3 AFM-based indentation on Pt-BMG. **a** Force F vs penetration depth h curves measured with five different maximum loads (180–1180 nN) using a diamond tip referred to in the text as tip #1. Despite carrying out the indents at different locations on the sample surface, all curves overlap perfectly within the accuracy of the measurement, indicating both that local changes in mechanical properties are negligible as well as that reproducibility of the measurement is high. From fitting the part of the curves before the easily visible kink with Eq. (1) (dashed blue curve), a tip radius of ≈ 4.1 nm is obtained. **b, c** AFM indents carried out following the same protocol as in **a**, but with different tips and on different locations. All curves exhibit the same overall behavior as in **a**, thereby confirming the validity of the approach. From fitting the data again with Eq. (1), the radius for tip #2 of **b** was determined as $R \approx 4.5$ nm and the one for tip #3 in **c** as $R \approx 6.1$ nm. **d–f** Mean contact pressure P_m vs penetration depth h curves. Curves in **d–f** were derived from the data shown in **a–c** using Eq. (2). AFM images acquired before and after performing indentation experiments. **g** Topography of the pristine Pt-BMG surface on sample #2. The stepped surface structure imposed onto the BMG sample by the STO single crystal mold is clearly visible¹⁵. **h** Same location as in **g**, but after AFM indentation tests using diamond tip #2 have been carried out. The locations of individual indents are highlighted by dashed circles and labeled with the peak load reached during the experiment. Although no pile up is visible for a 280 nN peak load, higher peak loads clearly lead to larger pile ups around the indent.

As long as h and F are lower than certain critical values h_y and F_y , dF/dh is comparatively high, meaning that the contact stiffness between tip and BMG is high. This segment can be fitted using Hertz' model (blue dashed line; see Eq. (1) in the Materials and Methods section), which results in the best matches when using tip radii of 4.1 nm (tip #1, panel a), 4.5 nm (tip #2, panel b), and 6.1 nm (tip #3, panel c), respectively. For the second segment where h and F exceed h_y and F_y , the load increases linearly with penetration depth, i.e., dF/dh (and thus the contact stiffness) takes on a constant, but smaller value, which is indicative of plastic flow. In addition, if loading proceeds past the critical point given by h_y and F_y , residual depths are observed upon unloading,

thereby corroborating the occurrence of plastic deformation in this regime. Figure 3d–f then show the mean contact pressure P_m as a function of the indentation depth h on Pt-BMG for the various maximum loads for the three tips.

For a more-detailed insight into the effect of the plastic flow, images acquired before and after the AFM indentation experiments of Fig. 3b, e are shown in Fig. 3g, h, respectively. In both images, the virtually atomically flat terraces formed by replicating the STO substrates' surface structure can be clearly identified, whereas the after image reveals in addition the indentation impressions from the experiments, arranged in two distinct rows. At 228 nN peak load, no pile up was observed around the location

of the indent in the post indentation AFM topography scans, indicating that only elastic deformation may have occurred, which is in good agreement with the findings in Fig. 3b. Loads higher than 228 nN, however, produce indentation impressions (i.e., the formation of a central hole surrounded by pile up), giving visual proof that indeed plastic has deformation occurred. Note that to check on reproducibility, we have for each of the data sets of Fig. 3 carried out two sets of indentation experiments, always starting from lower maximum forces to higher maximum forces. The curves for the two runs whose indents are depicted in the top and bottom rows of Fig. 3g are shown in supplementary Fig. 2, demonstrating that the experiments are highly reproducible.

Studying plastic deformation with increasingly smaller stressed volumes. For the analysis of the deformation behavior observed in Figs. 1 and 3, let us start by recalling the shear transformation zone (STZ) model proposed by Argon². Widely used to envision the origin of plastic deformation in metallic glasses at the atomic scale, it envisions a collective, non-affine shearing of atoms groups with zone sizes and strain being inherent to the structure of the glass. An STZ represents a cooperative rearrangement of a group of atoms overcoming the energy barrier that prevents local plastic flow, which is activated by an imposed stress tensor. The nucleation of STZs is an inelastic process and considered as representing the most elementary event of plastic flow in BMGs at the atomic scale⁹. Provided that the stressed volume is large enough, potential STZs that initially develop stochastically and independently from each other gradually become correlated by first aligning along directions dictated by the externally imposed stress, then forming a shear band nucleus, and eventually assembling into a complete shear band whose coordinated motion rapidly traverses through the specimen, thereby producing the plastic flow that manifests as pop-ins or serrations as seen in Fig. 1a. Even though the size (diameter) of STZs may cover a wide spectrum starting at individual atoms^{36,37}, average diameters of 1–2 nm have been suggested for Pt-BMGs based on rate-jump nanoindentation experiments²⁴. By reviewing both experimental and theoretical results, Zhang and Greer reasoned for the thickness of a shear band to be 10–20 nm³⁸, which means that a band's cross-section likely accommodates multiple STZs.

Although this STZ-shear band model is able to explain both the macroscopic deformation behavior of BMGs as well as the increase of yield stress that coincides with a reduction of the stressed volume, we have already pointed out in the introduction that it is not well understood what happens when the stressed volume becomes too small for a single shear band to form. To gain insight, experiments employing tensile^{39–42} or compression^{43–45} testing have been performed where the diameters of the specimen (rods for tensile testing, pillars for compression testing) were reduced to somewhere in the range of 20–400 nm, leading to volumes experiencing a stress high enough to induce flow anywhere from $\approx 10^4$ – 10^8 nm³. Yielding events, and thus plastic flow, were then found to occur prior to the formation of a complete shear band even though under idealized circumstances, a volume of $\approx 10^3$ nm³ would be sufficient for bands to take shape¹³. As possible mechanism, spread-out shear transformations have been suggested⁴¹, which ultimately lead to non-localized plastic flow at room temperature. The plastic deformation occurring under these conditions has then been described as homogeneous in the sense that “flow carriers are active everywhere even though they themselves are discrete”⁴⁴.

Despite these prior studies, multiple issues remain unresolved owing to experimental deficiencies (see, e.g., ref. 46). (i) Most previous research has been done on samples produced using focused ion beam (FIB) techniques, and the deformation of nanoscale samples has frequently been studied under an electron

beam. FIB milling leads, however, to irradiation damage that may influence plastic flow owing to stress localization, which may be particularly noticeable owing to the large surface-to-volume ratio of these samples. In addition, ion implanting or the creation of “defects” (such as a locally increased free volume) may change the mechanical properties of a surface layer of these small samples, and non-ideal geometries such as production-related deviations from a perfectly round or rectangular geometry or a tapering may play a role in the observed plastic flow behavior as well. For example, taper angles as small as 2° have been shown to lead to artifacts¹³. Similarly, the energetic electron beam used to study nanoscale deformation may cause local heating affecting plastic flow behavior, irradiation damage leading to small-scale stress localization, and electron beam-assisted diffusion. (ii) The large surface-to-volume ratio of these samples may result in an enhanced contribution of surface diffusion, thereby assisting apparent homogeneous deformation, which would not occur if a similarly sized stressed volume were located within the bulk. (iii) Finally, even if we assume the volume on an individual STZ to be as large as a couple of nm^{3,24}, the smallest volume probed in the previous studies still fits a couple of thousands of STZs, allowing them to engage in coordinated behavior featuring a certain degree of stress localization. In contrast, our experiments of Fig. 3 not only result in stressed volumes that are several orders of magnitude smaller than the ones probed with conventional setups, but they also avoid uncertainties due to above's points (i–iii), as sample preparation involves no exposure to an ion or electron beam, there are no geometrical uncertainties, and the small surface area of the stressed volume ensures that most flow occurs within the bulk. Its most notable characteristics are discussed in the following.

Yield shear stress τ_y as a function of volume affected by stress.

From the data in Fig. 3d–f, we deduce that the critical contact pressure at which yielding occurs is somewhere within a 20.2–25.2 GPa band for the three tips used, which means that the maximum yield stress τ_y ranges from 8.9–11.2 GPa or $G/4.1$ – $G/3.3$. With these values being markedly higher than the $G/11$ – $G/8$ band shown in Fig. 1b, it corroborates the trend pointed out in the introduction, namely that when either tensile or compressive stress gets localized in smaller and smaller volumes, higher and higher yield stresses are found as decreasing the volume reduces both the number of shear bands that are able to nucleate as well as the number of “defects” that localize and promote shear band nucleation and growth in the first place. As we are dealing with glasses, “defects” are usually equated with larger-than-average free volume, which reduces coherence while at the same time enabling increased flexibility for atom rearrangements needed to nucleate STZs and shear bands. As a consequence, fewer defects in the stressed volume directly result in higher yield stresses.

A comprehensive review of this effect was presented in 2014 by Nachum and Greer¹¹, where they found that when normalizing the pressure, at which yielding occurs with bulk values, deviations can be detected for indenter radii below ≈ 1 mm that follow a roughly double logarithmic scaling law independent of the exact composition of the glass. Figure 4 combines their and our findings, with all data taken from their paper except the data points representing Pt_{57.5}Cu_{14.7}Ni_{5.3}P_{22.5} (green hexagons), which are from the present work. In addition, the magenta dashed line reproduces the linear fit curve Nachum and Greer calculated, whereas the purple line represents the linear fit curve we obtain using just Pt-BMG. Most notably, both our data as well as the resulting fit match excellently with the trends uncovered by Nachum and Greer; this applies for both the averaged values from conventional nanoindentation ($\approx G/9$, $\approx G/12$, and $\approx G/16$ for the

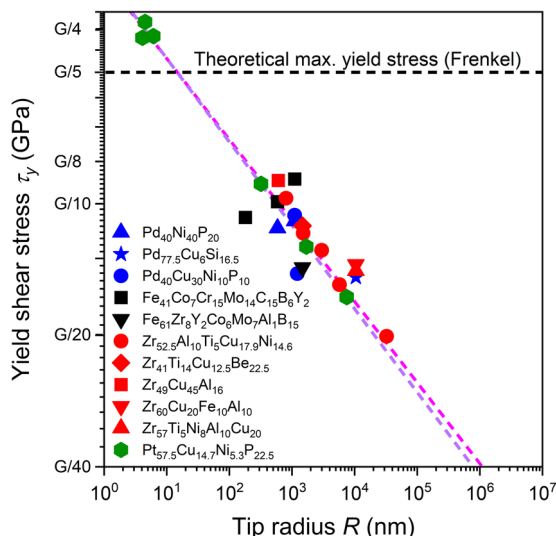


Fig. 4 Yield shear stress τ_y as a function of indenter radius R . Plot of τ_y in fractions of the shear modulus G , with $G/40$ reflecting the material's bulk value. The green hexagons mark the results obtained on Pt_{57.5}Cu_{14.7}Ni_{5.3}P_{22.5} in this work while all other data points are taken from Fig. 2 in ref. 11. Note that the fit given in that reference, reflected by the dashed magenta line, coincides favorably with the dashed purple line we find using Pt-BMG data only.

$R \approx 320$ nm, $R \approx 1.7$ μ m and $R \approx 7.5$ μ m tips, respectively) as well as for the $G/4.1$ – $G/3.3$ (i.e., $\tau_y \approx 8.9$ – 11.2 GPa) values found with AFM indentation.

For a more-detailed discussion, let us recall the arguments of the previous section according to which the plastic deformation of BMGs is accomplished for large enough stressed volumes through the formation and cooperative shearing of STZs. Thereby, the idea is that once an applied shear stress is higher than a certain critical value, an increasing number of STZs will nucleate at suitable free volume sites without significant atomic rearrangements in their surrounding glassy matrix⁴². When the high shear stress is constantly applied, STZs that have formed close to each other are continuously evolving and transforming to ultimately create a “shear band embryo” comprised by these local STZs^{44,47}. Finally, once the shear strain with a critical number of STZs reaches a location- and material-specific yield value in the incipient zone, the shear band starts to propagate, which is indicated in conventional nanoindentation by the observation of the first pop-in event. All data points in Fig. 4 obtained with tips featuring radii ranged between 10^2 nm and 10^5 nm are expected to follow such a deformation mechanism.

In this work, however, we are not just interested what happens when the volume exposed to critical stress is so small that a single shear band cannot be accommodated; the AFM indentation experiments shown in the results parts feature probing volumes that are at least two orders of magnitude smaller than required for shear band formation, being so small that not even a substantial number of STZs can fit. Thereby, the indenter radius was reduced to only a couple of nanometers and the yielding occurred when penetration depth was only at ≈ 1.3 – 1.4 nm. Under these circumstances, one can estimate (cf. Materials and Methods) a stressed volume where the stress is at least 50% of the max. shear stress of ≈ 15 nm³ when the experimental load reaches a value of ~ 330 nN (first yield for tip #1). This equates to the volume occupied by only a couple of “conventional” STZs (≈ 3 if we assume an average STZ volume of ~ 5 – 7 nm³ for a Pt-BMG²⁴) or as little as 1000 atoms that are critically affected by stress at the onset of deformation. Given that for such small volumes the shear

band-based deformation mechanism must break down, it is remarkable to discover that the dependence of the yield shear stress τ_y vs tip radius nevertheless follows the same linear trend as it does for the larger ones.

Variation and upper limit of the yield shear stress. Another finding worth noting is that in Fig. 3, all loading curves for each tip overlap despite having been carried out at different locations on the different samples. This suggests that structural inhomogeneities may not play a significant role in plastic deformation at the atomic scale for samples prepared similar to the ones in this study, a conclusion that is additionally supported both by the featureless contrast in the phase image Fig. 2b. Together, these results suggest that variations in BMG properties are much smaller than previously anticipated, which implies that the length scale of heterogeneities is smaller than anticipated as well^{20,21,48}. This is further corroborated by the fact that the yield shear stress τ_y was found to be pretty reproducible within $\sim \pm 10\%$ ($\tau_y \approx 8.9$ – 11.2 GPa $\approx G/4.1$ – $G/3.3$) for different tips and different samples. Interestingly, these values are higher than the presumed ‘theoretical maximum yield shear stress’ τ_{\max} , which, following arguments originally made by Frenkel⁴⁹, is believed to be $\approx G/5$ ¹⁰. One explanation for this finding could be that in Frenkel’s formula, the shear modulus is supposed to accurately reflect the shear of defect-free volumes containing only a small number of atoms (“ G_{theo} ”). The value of $G = 37.8$ GPa used throughout the paper, however, is derived from a much more macroscopic experiment (“ G_{mac} ”) and is therefore prone to be affected by the occurrence of “defects” (excess free volume for glasses) within the probed volume. As a result, $G_{\text{mac}} < G_{\text{theo}}$, and for τ_y values obtained during AFM indentation, G_{theo}/τ_y may still be larger than Frenkel’s estimated lower boundary of ≈ 5 even though $G_{\text{mac}}/\tau_y < 5$.

Homogeneous plastic flow at the atomic scale. Let us now turn our attention to the nature of the flow mechanism in place during AFM nanoindentation. As evident from Fig. 3, no pop-in events occur in the F – d curves, which suggests that the atomic-scale flow is homogeneous. As a first step, we checked whether some or all of the occurrence of homogeneous plastic flow can be attributed predominantly to the small radius of the AFM tip and resulting small probing volume as opposed to a combination of small volume and the glassy structure of the alloy. Towards this end, we have carried out complementary AFM-based indentation on a (111)-oriented platinum single crystal, a choice guided by the need for a model system that features similar atomic species while being structurally distinct from the disordered Pt-BMG. After preparation in ultrahigh vacuum by cycles of argon sputtering/annealing at 1000 °C, the platinum crystal featured atomically flat terraces with widths of ≈ 50 – 100 nm; RMS roughness on the terraces was observed to be identical to the one on the Pt-BMGs within the margin of accuracy of the measurement.

The comparison between F – h loading curves obtained on Pt-BMG with tip #2 and on the Pt(111) sample using a different diamond tip (“tip #4”) are shown in Fig. 5. When F and h were lower than their yield values F_y and h_y , the respective curve segments can be fitted with Hertz’ model Eq. (1) for both Pt-BMG and Pt(111). However, once yielding occurs, highly serrated fluctuations were observed in loading curves on the crystalline platinum (“pop-ins”). In agreement with observations on other crystalline materials^{33,34}, this finding indicates inhomogeneous atomic-scale plastic flow, which is known to be owing to the homogeneous nucleation of one or several dislocations from a flaw-free crystalline structure followed by instantaneous slip events along slip planes and slip lines^{50,51}. From the related theory, the length of each pop-in on Pt(111) can be determined as

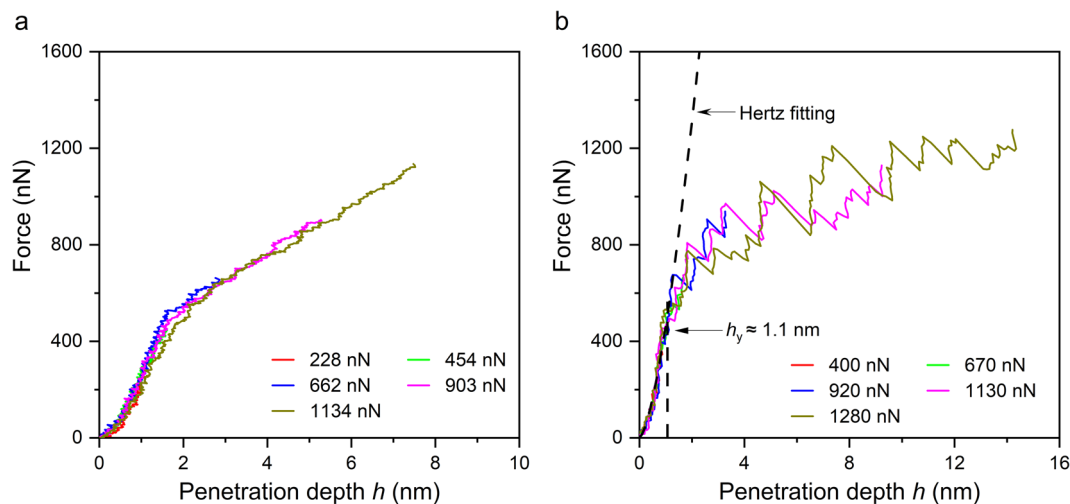


Fig. 5 Homogeneous vs inhomogeneous atomic-scale flow. Force vs penetration depth curves **a** on Pt-BMG using diamond tip #2 and **(B)** on Pt(111) with diamond tip #4. From the Hertz fit in **b** and with assuming $E_{\text{Pt}(111)} = 168$ GPa and $\nu_{\text{Pt}(111)} = 0.38$, the radius of tip #4's apex can be extracted as ≈ 4.5 nm, thereby matching well with the radii obtained for tips #1-3.

integer multiples of the minimum slip distance in z direction (≈ 2 Å). Corroborating the picture of glide plane activation even during atomic-scale plastic flow is the fact that the material pile-up around the indentation holes on the Pt(111) surfaces was oriented (Supplementary Fig. 3), likely following specific glide planes or crystallographic directions. In contrast, the pile-up on the BMGs appears mostly uniform (cf. Figure 3h).

Next, we tested how the flow depends on the loading rate, which we have seen to change from smooth at high speeds to serrated at low speeds during conventional nanoindentation (Supplementary Fig. 1), indicating inhomogeneous flow in agreement with the formation of shear bands. But even though loading rates during AFM indentation are 10–200 \times slower than during conventional nanoindentation, which should favor serration if it were to occur, no serrated plastic flow was observed (Supplementary Fig. 4). This implies that plastic flow in AFM indentation is indeed homogeneous and proceeds without causing the formation of a shear band.

But what exactly is the nature of the observed homogeneous flow? Recalling above's arguments, non-localized plastic flow requires “spread-out shear transformations”⁴¹ and flow carriers that “are active everywhere even though they themselves are discrete”⁴⁴. Close to the glass transition temperature, BMGs are known to exhibit homogeneous plastic deformation via viscous flow^{3,52}, in which case the flow carriers are identified as individual atoms and the spread-out shear transformations are “liquid-like” rearrangements of these atoms. As we are well below the material's glass transition temperature of $T_g = 233$ °C⁵³, groups of atoms are likely to at least temporarily travel together as they do in the STZ model (i.e., the flow carriers may be larger than individual atoms), but due to the small activated volume and the need to fit many such STZs into it, they need to be much smaller than the average value of 5–7 nm³ suggested for STZs during macroscopic deformation in ref. 24. A recent molecular dynamics simulation of a tip with 4 nm radius indenting a Cu₅₀Zr₅₀ glass⁵⁴ identifies such “small STZs” as only 1–2 atoms thick in directions parallel to the surface even though they can be more extended perpendicular to it. Similarly, Guo et al.³⁹ speculate that the spread-out nature of the flow in such small dimensions is due to the low probability of finding “pre-damaged fertile sites” that could lead to shear localization, under which circumstances a re-distribution of free volume will occur in “dislocation-like” shear events happening all over the small volume that “seem

homogeneous”, whereas Luo et al.⁴⁰ consider “modest-range strain relaxation via atom diffusion”. Finally, Liu et al.⁵⁵ have recently examined atomic-scale structural heterogeneity in a BMG near surfaces and its reorganization during bending using a synchrotron diffraction technique. Their study finds that the glass' heterogeneous short-range atomic arrangements change during deformation, an observation that may in some cases reflect the relative movement of atoms in a fashion that could be interpreted as “small STZ motion” or, in other instances, would allow the formation of small, but temporally transient STZs. A sketch illustrating a possible mechanism for atomic-scale homogeneous plastic flow that is consistent with our findings is displayed in Fig. 6.

Let us end with a comment on surface vs bulk properties. Since during AFM-based indentation, only a very small number of atoms are being affected, one could wonder whether the mechanism proposed in Fig. 6 is actually a “bulk” mechanism or whether the occurrence of the atomic-scale homogeneous flow requires proximity to the surface. Although pile-up is certainly only going to happen at the surface, the very fact that the flow is homogeneous and “spread-out” nevertheless indicates that the main effect is a volume effect rather than a surface effect, as the proposed “small STZ” mechanism of Fig. 6 does not require the proximity of any surface. Rather, the only requirement of the proposed mechanism to occur appears to be the fact that the overall stressed volume is kept small enough to prevent shear localization.

The atomic-scale plastic flow of a platinum-based metallic glass was investigated by indenting the surface with the tip on an AFM. Thanks to the application of a unique sample preparation technique that yields virtually atomically flat and structurally homogeneous surfaces, indents of only a few nanometers could be reproducibly analyzed. This offers access to the plastic flow characteristics of sample volumes containing as little as 1000 atoms, providing results that are unaltered by the effects of surface diffusion, electron beam damage, or excess surface roughness that have plagued alternate approaches in the past. Thereby, a yield stress was measured that is not only significantly higher than the values derived from conventional nanoindentation, but remarkably close to the predicted maximum. In striking contrast to both the flow of the Pt-BMG on mesoscopic and macroscopic scales, which is accommodated by shear bands, and the flow of single-crystalline platinum, which is at all scales

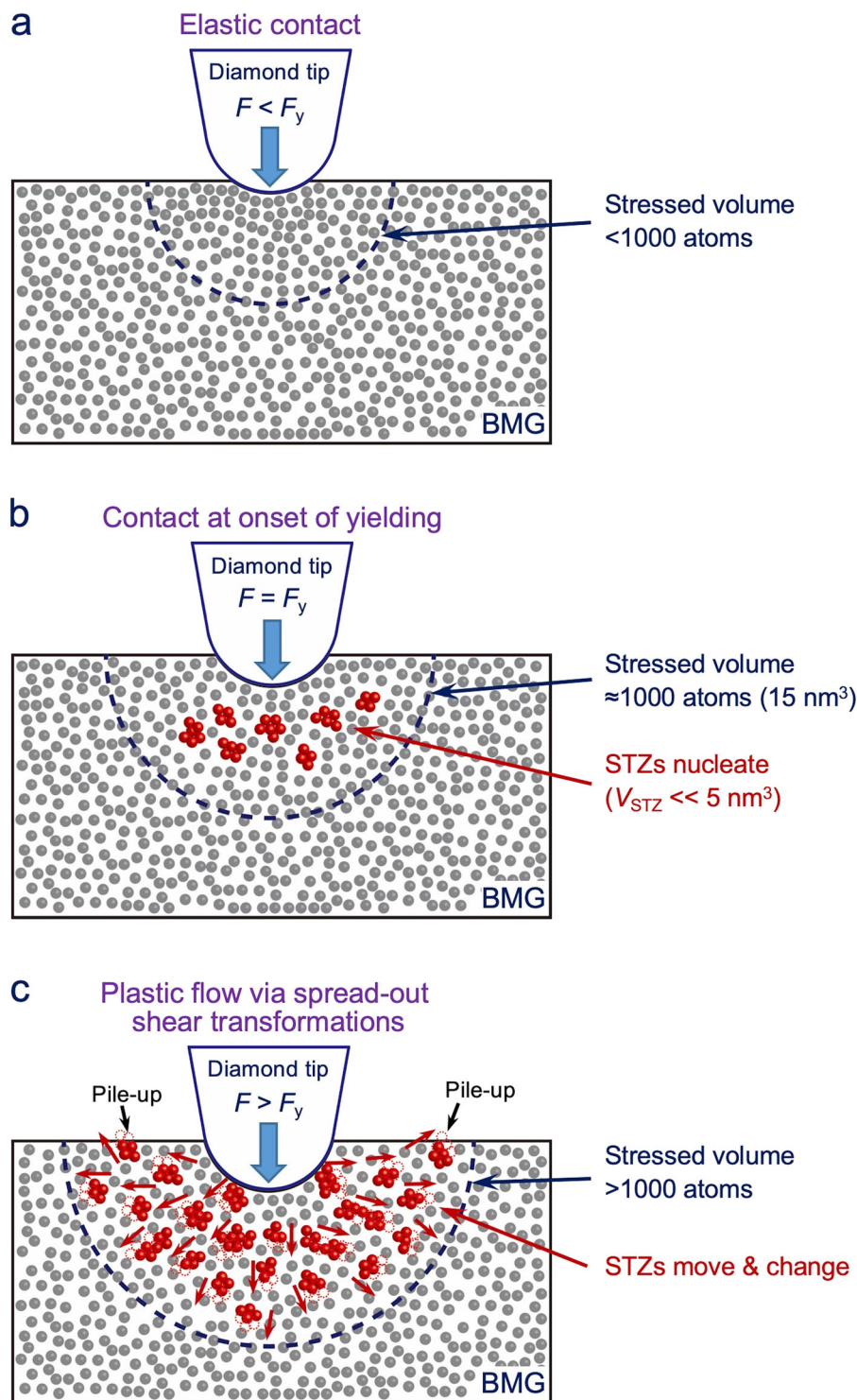


Fig. 6 Sketches illustrating a possible mechanism of atomic-scale plastic flow consistent with the experimental findings of this paper. **a** A diamond tip with very small radius (some nm) is indenting a sample of bulk metallic glass below the material's yield point. In this case, deformation can be well described by the Hertz model, and much <1000 atoms are exposed to significant stress levels. **b** Near the onset of yielding, the volume where atoms are subjected to a stress sufficient to induce positional changes approaches $\approx 15 \text{ nm}^3$, comprising ≈ 1000 atoms. At this stage in the process, the atomic-level heterogeneity intrinsic to any glass due to its structural disorder allows small STZs consisting out of only few atoms to nucleate via small displacements in atomic locations. **c** Once enough STZ have formed, they move without leading to significant degrees of shear localization. Note, in particular, that these STZs are expected to be transient in its temporal nature, which additionally prevents appreciative degrees of shear localization.

mediated by dislocations and glide planes, the atomic-scale deformation of the Pt-BMG is found to be homogeneous even though experiments were carried out far below the material's glass transition temperature. This behavior is attributed to the

fact that the volume critically affected by the external stress is insufficient to support a shear localization sufficient to enable the formation of a shear band. Instead, a picture emerged that includes spread-out flow carriers that are spatially and temporally

fluid while featuring an average overall size that is substantially smaller than for the “regular” STZs encountered during macroscopic deformation, characteristics that ultimately lead to the observed homogeneous flow. In addition, results indicate that materials properties such as free volume or yield stress do not appear to fluctuate on a length scale affected by such indents, which is of importance when attempting to develop structure-property-processing relationships for metallic glasses.

Methods

Sample preparation. The composition of the BMG used in this research was $\text{Pt}_{57.5}\text{Cu}_{14.7}\text{Ni}_{5.3}\text{P}_{22.5}$, which is referred to as Pt-BMG throughout the paper. The alloy was prepared by casting followed by water quenching⁵⁶ and its amorphous structure was subsequently confirmed by X-ray diffraction. Thermoplastic forming with SrTiO_3 (STO) as a substrate was then used to produce atomically flat Pt-BMG surfaces that reflected a mirror image of the STO single crystals used as molds; for details, see ref. 15. In short, STO crystals with (100) orientation provided by MTI Corporation (Richmond, CA) were annealed in the air under oxygen flow at 1000 °C for 2 hours, after which they feature atomically flat terraces ≈ 50 –400 nm in width that are separated by one-unit-cell high steps (0.39 nm). Subsequently, (i) the STO was introduced into a custom-designed press; (ii) an as-cast Pt-BMG ingot was placed on top of it; (iii) both were heated to 270 °C; (iv) the pressure was ramped up; and (v) once the pressure was released, the thermal mismatch between the substrate and the sample caused the formed Pt-BMG disc to separate from the STO. In this context, please note that since the sample is being kept at maximum pressure for three minutes while being heated to a temperature of 270 °C at which relaxation times are less than a second⁵⁷, we do not expect residual surface stresses to be present that would substantially influence the results of surface hardness or indentation measurements carried out after cooling.

Special attention was given to characterize the surface chemistry and potential oxide formation using x-ray photoelectron spectroscopy. The data obtained suggest that indeed some oxide formation occurs on the surface, which is identified as overwhelmingly phosphate (P-O). This causes the immediate surface layer to be somewhat P-enriched compared with the composition in the bulk, driven by the exposition of surface atom to air either after the separation of the BMG replica from the mold or during the imprinting process itself. However, sputtering in vacuum with Ar gas reveals that after ≈ 1 nm of surface material has been removed, oxides have virtually vanished, and prolonged sputtering confirms that the elementary distribution subsequently remains stable with depth. As a consequence, indentations of depths >1 nm are expected to penetrate material that in its structure and composition is largely identical to the alloy’s bulk.

Conventional nanoindentation testing. Bulk Young’s modulus of atomically flat Pt-BMG made using the thermoplastic forming method outlined above was measured using a NanoIndenter G200 (Keysight Technologies, Santa Rosa, CA, USA) fitted with a Berkovich tip. Using the same instrument and identically prepared samples, additional spherical indentation experiments were performed using a diamond tip of radius ≈ 320 nm to study the elastic–plastic transition using basic loading–unloading. Finally, complementary testing using spherical diamond tips of nominal radii ≈ 1.7 μm and ≈ 7.5 μm (Synton MDP LTD, Nidau, Switzerland; tip radii calibrated using single-crystalline tungsten) was carried out with an MTS nanoindenter XP (MTS Systems Corporation, Eden Prairie, NM, USA). Owing to the considerably larger indent depth, Pt-BMG samples thermoplastically formed at 270 °C were first polished using standard metallographic sample preparation techniques followed by 48 h in a vibratory polisher in non-crystallizing colloidal silica solution. A method based on a constant strain rate of 0.05 was used to analyze these samples⁵⁸.

AFM imaging and AFM-based indentation testing. Both the characterization of the surface quality and the atomic-scale indentation testing were performed at room temperature in air with a Nanoscope Multimode AFM equipped with a Nanoscope III electronics (Bruker Nano Surfaces, Santa Barbara, CA, USA). Experiments limited to tapping-mode imaging only (e.g., Fig. 2) used PPP-NCL-50 silicon cantilevers (Nanosensors, Neuchâtel, Switzerland), whereas all testing that included indenting the sample (such as in Figs. 3 and 5) was carried out with diamond-coated silicon tips purchased from Adama Innovations, Dublin, Ireland. Adama Innovations specified all tips to be cone-shaped with cone half angles of $15^\circ \pm 2^\circ$ and spherical apices with radii lower than 10 nm; in addition, they estimate Young’s modulus of the diamond tips to be between 850 and 950 GPa. We found that tip radii were indeed not only lower than this value, but so small that we could not reliably quantify them with scanning electron microscopy owing to the fact that the diamond produced poor contrast during imaging at this length scale. The spring constants of the cantilevers were verified using a tipless calibration cantilever with a force constant of 12.96 N/m (CLFC-NOBO, Bruker, USA) to be within a ≈ 47 –52 N/m range. After nanoindentation, the topography of the indented area was scanned with the same tip used for indentation while operating the microscope in tapping mode.

Recovering force-penetration depth curves. In an AFM indentation test, the relationship between the cantilever deflection d and the piezo extension displacement z can be obtained^{31,59}. d was calibrated by measuring the cantilever displacement vs the piezo extension displacement on a sapphire surface (MTI Corporation, Richmond, CA, USA, a-plane orientation). For cantilevers with spring constants as used here, the sapphire surface is only negligibly deformed even when the piezo is maximally extended during a typical approach curve. The distance the piezo has traveled between when the tip makes contact with the surface and the point of maximum extension corresponds therefore in good approximation to the cantilever’s total displacement, resulting in an effective calibration of the cantilever deflection d . The applied force F can then be calculated from $F = kd$, where k is the spring constant of cantilever while the penetration depth h can be recovered using $h = z - d$. As an example, Supplementary Fig. 5a shows typical d vs z curves on Pt-BMG and sapphire. After the calibration using the d - z curve obtained on sapphire, the relationship between applied load and penetration depth (F - h curve) for Pt-BMG is extracted, as shown in Supplementary Fig. 5b. In this investigation, the atomic-scale plastic deformation of sample surfaces was analyzed based on the d - z curves recorded in AFM nanoindentation that were subsequently converted to represent F - h curves.

Adjusting loading rates. During an AFM indentation, the loading–unloading period can only be controlled by setting the duration of the total piezo extension–retraction cycle. However, As each such cycle starts with the tip away from the surface, the duration of the loading and unloading part of the total extension–retraction cycle (i.e., the part where the tip is in actual physical contact with the surface) was always shorter than the duration of an individual complete piezo extension–retraction cycle. Unless explicitly mentioned, the extension–retraction duration of piezo was set to 1 s in this investigation and the data acquisition rate 512 points per second; by controlling the ratio of piezo extension and cantilever deflection displacement, the loading rate was nevertheless controlled to be within a range of ≈ 1.8 –4.6 μNs^{-1} . Interestingly, we find that the loading rate increases almost linearly with penetration depth until the critical value h_c is reached, after which it stays relatively unchanged at a constant value around which is fluctuates by 10–20%. In addition, in order to understand the effect of loading rate on the plastic flow of Pt-BMG, the duration of the complete piezo extension–retraction cycles were varied separately from 0.5 to 10 s, resulting in loading rates ranging from 2.9 μNs^{-1} to 58 μNs^{-1} (Supplementary Fig. 4). In these experiments, the load was increased until a maximum load of 1670 μN was reached. To further minimize piezoelectric creep effects during loading rate-dependent measurements, a piezo drift correction was performed employing a method proposed by Caron et al.³⁵ specifically for AFM experiments on metallic glasses.

Stress and pressure calculations during spherical indentation. The load–penetration depth curves during a spherical indentation experiment can be analyzed using Hertzian contact theory⁶⁰, which assumes a frictionless contact between two elastically isotropic solids. In the case of purely elastic deformation, the relationship between the load F and the penetration depth h is then given by²⁶

$$F = \frac{4}{3} E^* R^{1/2} h^{3/2}, \quad (1)$$

where R is the effective tip radius and $E^* = ((1 - \nu_{\text{tip}}^2)/E_{\text{tip}} + (1 - \nu_{\text{BMG}}^2)/E_{\text{BMG}})^{-1}$ the reduced modulus with E_{tip} , E_{BMG} reflecting the elastic moduli and ν_{tip} , ν_{BMG} representing Poisson’s ratio of the tip material and the Pt-BMG, respectively. $E_{\text{BMG}} = 105$ GPa and $\nu_{\text{BMG}} = 0.39$ were already given in the main text; for the diamond-related values, we used for E_{tip} the average value of the range specified by the manufacturer of the tips (i.e., $E_{\text{tip}} = 900$ GPa) when analyzing the AFM indentation testing data instead of the standard literature value of $E_{\text{tip}} = 1141$ GPa for bulk diamond, which was utilized for analyzing the experimental data obtained by conventional nanoindentation. For ν_{tip} , however, the diamond bulk value of 0.07 was employed for ν_{tip} in all cases. The Hertz mean contact pressure P_m and prior to a yielding load F_y can be described by

$$P_m = \left(\frac{16 FE_y^2}{9\pi^3 R^2} \right)^{1/3}, \quad (2)$$

from which we can deduce the yield shear stress τ_y occurring at the first yield event using^{8,26}

$$\tau_y = 0.445 P_m, \quad (3)$$

When using this approach, one should note four important points:

- (i) The radius of the tips was estimated by plotting force and penetration depth data as F vs $h^{3/2}$, which according to Eq. (1) results in a straight line whose slope provides an estimate of the tip radius if we introduce E^* as defined in the previous paragraph⁶¹. As at very low indentation depths (<0.2 nm) as well as when getting close to the material’s yield force the data are not very reliable, only data from 25% yield force values to 80 % yield force values was used to estimate the radius.

- (ii) As pointed out above, Eq. (2) is only correct until yielding occurs. After that, the contact area between tip and sample will inevitably be larger as predicted by the Hertz model, both owing to a sink-in effect into the sample as well as owing to the occurrence of pile up around the indent (cf. Figure 3h). As a consequence, values obtained for P_m past yielding using Eq. (2) will reflect an upper boundary for the actual value. At the same time, it is unlikely that yield pressure will drop during the deformation process; in contrast, some degree of shear strengthening is expected⁶². Therefore, P_m at yield should represent a lower boundary for the actual mean pressure past yielding.
- (iii) On top of the arguments given in point (ii), additional uncertainties arise once the tip has penetrated the surface to a point where the contact geometry transitions from a sphere to a cone, assuming that the tip shape is indeed sphero-conical as specified by the manufacturer. Using simple geometry, we find that this is the case when $h_c \geq R(1 - \sin\theta)$, where θ is the cone $\frac{1}{2}$ angle and h_c the contact depth, i.e., the depth where the sphere and the indented surface are actually in intimate contact. For a spherical indentation experiment carried out in the elastic regime, Hertzian theory reveals that h_c is half the total indentation depth h ²⁶ while in the elastic-plastic regime, it can be calculated using the Oliver-Pharr model

$$h_c = h - (\varepsilon F/S), \quad (4)$$

where h is the total measured penetration depth, ε is an indenter geometry-based constant that is 0.75 for a sphere, and S is the elastic contact stiffness⁶³. As S is unknown in the AFM indentation experiments performed, it is, however, not possible to calculate the contact depth accurately during an indentation experiment accurately after yielding occurs. For a rough approximation, we work with the assumption that the contact depth h_c is even past yield still half of the penetration depth h . When doing so, we find that at the maximum penetration depths h achieved during the experiments described in the main text, the tip-sample contact is either well described with a sphere-flat model or it is sufficiently close to the sphere-conical transition depth that it can be justified to still use the sphere-flat model.

Finally, it should be pointed out that even though we are using Hertz model-based Eq. (2) for our data analysis, we appreciate that further uncertainties arise from the fact that Hertz's model is only a good solution in the regime where the contact radius r is small compared with tip radius R , which may not be the case for some of the deeper indents carried out.

Stressed volume estimation during spherical indentation. Assuming that the tip is spherical and rotationally symmetric, the contact radius at yield can be calculated as $a = \sqrt{3FR/4E^*}$ ^{26,28}. Even though the stress field underneath the indenter is complex, the volume that is critically affected by the stress field can be estimated analytically using approximations, such as that the stress field extends up to a depth $2a$ underneath the indenter and that the maximum shear stress occurs approximately at a depth of $\approx 0.5a$. If we consider the stressed volume $V_{50} \approx 0.5\pi a^3$ where the shear stress is at least 50% of the maximum shear stress^{26,28}, the number of atoms in that volume N_{50} can be estimated by using the equation $N_{50} = V_{50}\rho N_A/A$, where A is the atomic mass (≈ 131 g/mol), N_A Avogadro's number, and ρ the density, which we measured as 15.1 g/cm³ using helium pycnometry. With these assumptions, the contact radius for tip #1 at yield ($F_y = 329$ nN) becomes $a \approx 2.1$ nm, hence $V_{50} \approx 14.6$ nm³, with which the number of atoms in the stressed volume at yield experiencing at least 50% of the maximum shear stress is ≈ 1000 .

Data availability

The data that support the results within this paper and other findings of this study are available from J.Y. on reasonable request.

Received: 7 September 2020; Accepted: 25 January 2021;

Published online: 26 February 2021

References

- Suryanarayana, C., Inoue, A. *Bulk Metallic Glasses*, 2nd edn. (CRC Press, 2017).
- Argon, A. S. Plastic deformation in metallic glasses. *Acta Metall.* **27**, 47–58 (1979).
- Schuh, C. A., Hufnagel, T. C. & Ramamurty, U. Mechanical behavior of amorphous alloys. *Acta Mater.* **55**, 4067–4109 (2007).
- Hufnagel, T. C., Schuh, C. A. & Falk, M. L. Deformation of metallic glasses: recent developments in theory, simulations, and experiments. *Acta Mater.* **109**, 375–393 (2016).
- Eckert, J., Das, J., Pauly, S. & Duhamel, C. Mechanical properties of bulk metallic glasses and composites. *MRS Bull.* **32**, 635–638 (2007).
- Greer, A. L., Castellero, A., Madge, S. V., Walker, I. T. & Wilde, J. R. Nanoindentation studies of shear banding in fully amorphous and partially devitrified metallic alloys. *Mater. Sci. Eng. A* **375–377**, 1182–1185 (2004).
- Burgess, T. & Ferry, M. Nanoindentation of metallic glasses. *Mater. Today* **12**, 24–32 (2009).
- Bei, H., Lu, Z. P. & George, E. P. Theoretical strength and the onset of plasticity in bulk metallic glasses investigated by nanoindentation with a spherical indenter. *Phys. Rev. Lett.* **93**, 125504 (2004).
- Greer, A. L., Cheng, Y. Q. & Ma, E. Shear bands in metallic glasses. *Mater. Sci. Eng. R Rep.* **74**, 71–132 (2013).
- Johnson, W. & Samwer, K. A universal criterion for plastic yielding of metallic glasses with a (T/T_g)^{2/3} temperature dependence. *Phys. Rev. Lett.* **95**, 195501 (2005).
- Nachum, S. & Greer, A. Indentation size effect in metallic glasses: mean pressure at the initiation of plastic flow. *J. Alloys Compounds* **615**, S98–S101 (2014).
- Choi, I.-C. et al. Indentation size effect and shear transformation zone size in a bulk metallic glass in two different structural states. *Acta Mater.* **60**, 6862–6868 (2012).
- Bharathula, A., Lee, S.-W., Wright, W. J. & Flores, K. M. Compression testing of metallic glass at small length scales: effects on deformation mode and stability. *Acta Mater.* **58**, 5789–5796 (2010).
- Schroers, J. & Johnson, W. L. Ductile bulk metallic glass. *Phys. Rev. Lett.* **93**, 255506 (2004).
- Li, R. et al. Atomic imprinting into metallic glasses. *Commun. Phys.* **1**, 75 (2018).
- Zhou, C. et al. Atomic imprinting in the absence of an intrinsic length scale. *Appl. Mater.* **8**, 011110 (2020).
- Spaepen, F. Homogeneous flow of metallic glasses: a free volume perspective. *Scripta Mater.* **54**, 363–367 (2006).
- Zhao, K., Xia, X., Bai, H., Zhao, D. & Wang, W. Room temperature homogeneous flow in a bulk metallic glass with low glass transition temperature. *Appl. Phys. Lett.* **98**, 141913 (2011).
- Lu, Z., Jiao, W., Wang, W. & Bai, H. Flow unit perspective on room temperature homogeneous plastic deformation in metallic glasses. *Phys. Rev. Lett.* **113**, 045501 (2014).
- Yang, Y. et al. Fractal growth of the dense-packing phase in annealed metallic glass imaged by high-resolution atomic force microscopy. *Acta Mater.* **60**, 5260–5272 (2012).
- Zeng, J. F. et al. On the use of atomic force microscopy for structural mapping of metallic-glass thin films. *Intermetallics* **44**, 121–127 (2014).
- Pan, J., Ivanov, Y. P., Zhou, W. H., Li, Y. & Greer, A. L. Strain-hardening and suppression of shear-banding in rejuvenated bulk metallic glass. *Nature* **578**, 559–562 (2020).
- Ketov, S. V. et al. Rejuvenation of metallic glasses by non-affine thermal strain. *Nature* **524**, 200–203 (2015).
- Pan, D., Inoue, A., Sakurai, T. & Chen, M. Experimental characterization of shear transformation zones for plastic flow of bulk metallic glasses. *Proc. Natl Acad. Sci.* **105**, 14769–14772 (2008).
- Perepezko, J. H., Imhoff, S. D., Chen, M. W., Wang, J. Q. & Gonzalez, S. Nucleation of shear bands in amorphous alloys. *Proc. National Acad. Sci. USA* **111**, 3938 (2014).
- Johnson, K. *Contact mechanics*. (Cambridge University Press, 1985).
- García, R. *Amplitude Modulation Atomic Force Microscopy*. (John Wiley & Sons, 2011).
- Wagner, H. et al. Local elastic properties of a metallic glass. *Nat. Mater.* **10**, 439 (2011).
- Lu, Y. et al. Structural signature of plasticity unveiled by nano-scale viscoelastic contact in a metallic glass. *Sci. Rep.* **6**, 29357 (2016).
- PFMTn, Arce, Riera, G. A., Gorostiza, P. & Sanz, F. Atomic-layer expulsion in nanoindentations on an ionic single crystal. *Appl. Phys. Lett.* **77**, 839–841 (2000).
- Caron, A. Quantitative hardness measurement by instrumented AFM-indentation. *J. Vis. Exp.* **117**, e54706 (2016).
- Paul, W., Oliver, D., Miyahara, Y. & Grütter, P. H. Minimum threshold for incipient plasticity in the atomic-scale nanoindentation of Au (111). *Phys. Rev. Lett.* **110**, 135506 (2013).
- Filleter, T. & Bennewitz, R. Nanometre-scale plasticity of Cu (100). *Nanotechnology* **18**, 044004 (2007).
- Egberts, P. & Bennewitz, R. Atomic-scale nanoindentation: detection and identification of single glide events in three dimensions by force microscopy. *Nanotechnology* **22**, 425703 (2011).
- Caron, A. & Bennewitz, R. Lower nanometer-scale size limit for the deformation of a metallic glass by shear transformations revealed by quantitative AFM indentation. *Beilstein J. Nanotechnol.* **6**, 1721–1732 (2015).
- Ju, J., Jang, D., Nwankpa, A. & Atzmon, M. An atomically quantized hierarchy of shear transformation zones in a metallic glass. *J. Appl. Phys.* **109**, 053522 (2011).
- Ju, J. & Atzmon, M. A comprehensive atomistic analysis of the experimental dynamic-mechanical response of a metallic glass. *Acta Mater.* **74**, 183–188 (2014).

38. Zhang, Y. & Greer, A. Thickness of shear bands in metallic glasses. *Appl. Phys. Lett.* **89**, 071907 (2006).
39. Guo, H. et al. Tensile ductility and necking of metallic glass. *Nat. Mater.* **6**, 735 (2007).
40. Luo, J., Wu, F., Huang, J., Wang, J. & Mao, S. Superelongation and atomic chain formation in nanosized metallic glass. *Phys. Rev. Lett.* **104**, 215503 (2010).
41. Deng, Q. et al. Uniform tensile elongation in framed submicron metallic glass specimen in the limit of suppressed shear banding. *Acta Mater.* **59**, 6511–6518 (2011).
42. Tian, L. et al. Approaching the ideal elastic limit of metallic glasses. *Nat. Commun.* **3**, 609 (2012).
43. Volkert, C., Donohue, A. & Spaepen, F. Effect of sample size on deformation in amorphous metals. *J. Appl. Phys.* **103**, 083539 (2008).
44. Shan, Z. et al. Plastic flow and failure resistance of metallic glass: Insight from in situ compression of nanopillars. *Phys. Rev. B* **77**, 155419 (2008).
45. Jang, D. & Greer, J. R. Transition from a strong-yet-brittle to a stronger-and-ductile state by size reduction of metallic glasses. *Nat. Mater.* **9**, 215–219 (2010).
46. Tian, L., Shan, Z.-W. & Ma, E. Ductile necking behavior of nanoscale metallic glasses under uniaxial tension at room temperature. *Acta Mater.* **61**, 4823–4830 (2013).
47. Shimizu, F., Ogata, S. & Li, J. Theory of shear banding in metallic glasses and molecular dynamics calculations. *Mater. Transact.* **48**, 2923–2927 (2007).
48. Liu, Y. et al. Characterization of nanoscale mechanical heterogeneity in a metallic glass by dynamic force microscopy. *Phys. Rev. Lett.* **106**, 125504 (2011).
49. Frenkel, J. Zur theorie der elastizitätsgrenze und der festigkeit kristallinischer körper. *Zeitschrift für Physik* **37**, 572–609 (1926).
50. Michalske, T. & Houston, J. Dislocation nucleation at nano-scale mechanical contacts. *Acta Mater.* **46**, 391–396 (1998).
51. Lilleodden, E., Zimmerman, J., Foiles, S. & Nix, W. Atomistic simulations of elastic deformation and dislocation nucleation during nanoindentation. *J. Mech. Phys. Solids* **51**, 901–920 (2003).
52. Inoue, A. Stabilization of metallic supercooled liquid and bulk amorphous alloys. *Acta Mater.* **48**, 279–306 (2000).
53. Schroers, J. & Johnson, W. L. Highly processable bulk metallic glass-forming alloys in the Pt–Co–Ni–Cu–P system. *Appl. Phys. Lett.* **84**, 3666–3668 (2004).
54. Qiu, C., Zhu, P., Fang, F., Yuan, D. & Shen, X. Study of nanoindentation behavior of amorphous alloy using molecular dynamics. *Appl. Surf. Sci.* **305**, 101–110 (2014).
55. Liu, S. N. et al. Deformation-enhanced hierarchical multiscale structure heterogeneity in a Pd–Si bulk metallic glass. *Acta Mater.* **200**, 42–55 (2020).
56. Schroers, J. Condensed-matter physics: glasses made from pure metals. *Nature* **512**, 142 (2014).
57. Ketkaew, J. et al. Mechanical glass transition revealed by the fracture toughness of metallic glasses. *Nat. Commun.* **9**, 3271 (2018).
58. Datye, A., Ketkaew, J., Schroers, J. & Schwarz, U. D. Effect of the fictive temperature on the modulus, hardness, yield strength, dynamic mechanical and creep response of $Zr_{44}Ti_{11}Cu_{10}Ni_{10}Be_{25}$ metallic glasses. *J. Alloys Compd.* **819**, 152979 (2019).
59. Asenjo, A., Jaafar, M., Carrasco, E. & Rojo, J. Dislocation mechanisms in the first stage of plasticity of nanoindented Au (111) surfaces. *Phys. Rev. B* **73**, 075431 (2006).
60. Hertz, H., Jones, D. E. & Schott, G. A. *Miscellaneous papers*. (Macmillan and Company, 1896).
61. Datye, A. et al. Extraction of anisotropic mechanical properties from nanoindentation of SiC-6H single crystals. *J. Appl. Mechanics* **83**, 091003 (2016).
62. Warren, O. L. et al. In situ nanoindentation in the TEM. *Mater. Today* **10**, 59–60 (2007).
63. Oliver, W. C. & Pharr, G. M. An improved technique for determining hardness and elastic modulus using load and displacement sensing indentation experiments. *J. Mater. Res.* **7**, 1564–1583 (1992).

Acknowledgements

We are grateful to Dr. S. Suib at the University of Connecticut for allowing the use of their equipment. We also acknowledge the support of scientists at Oak Ridge National Laboratory. We thank the Department of Energy for funding through Grant No. DE-SC0016179. Work carried out after 6/1/2019 was supported by the National Science Foundation Grant No. NSF CMMI-1901959. J.Y. was funded by the Natural Science Foundation of China No. 51975492.

Author contributions

U.D.S. conceived and directed the work and J.Y. and A.D. conducted and analyzed the experiments with support by Z.C., C.Z., O.E.D., and J.S. All authors collaborated to compose the manuscript.

Competing interests

The authors declare no competing financial interests.

Additional information

Supplementary information The online version contains supplementary material available at <https://doi.org/10.1038/s43246-021-00124-3>.

Correspondence and requests for materials should be addressed to J.Y. or U.D.S.

Peer review information Primary handling editor: John Plummer

Reprints and permission information is available at <http://www.nature.com/reprints>

Publisher's note Springer Nature remains neutral with regard to jurisdictional claims in published maps and institutional affiliations.



Open Access This article is licensed under a Creative Commons Attribution 4.0 International License, which permits use, sharing, adaptation, distribution and reproduction in any medium or format, as long as you give appropriate credit to the original author(s) and the source, provide a link to the Creative Commons license, and indicate if changes were made. The images or other third party material in this article are included in the article's Creative Commons license, unless indicated otherwise in a credit line to the material. If material is not included in the article's Creative Commons license and your intended use is not permitted by statutory regulation or exceeds the permitted use, you will need to obtain permission directly from the copyright holder. To view a copy of this license, visit <http://creativecommons.org/licenses/by/4.0/>.

© The Author(s) 2021